Electric field gradient focusing in microchannels with embedded bipolar electrode

Dzmitry Hlushkou,[a] Robbyn K. Perdue,[b] Rahul Dhopeshwarkar,[b] Richard M. Crooks*[b] and Ulrich Tallarek*[a]

Received 15th December 2008, Accepted 13th March 2009
First published as an Advance Article on the web 1st April 2009
DOI: 10.1039/b822404h

The complex interplay of electrophoretic, electroosmotic, bulk convective, and diffusive mass/charge transport in a hybrid poly(dimethylsiloxane) (PDMS)/glass microchannel with embedded floating electrode is analyzed. The thin floating electrode attached locally to the wall of the straight microchannel results in a redistribution of local field strength after the application of an external electric field. Together with bulk convection based on cathodic electroosmotic flow, an extended field gradient is formed in the anodic microchannel segment. It imparts a spatially dependent electrophoretic force on charged analytes and, in combination with the bulk convection, results in an electric field gradient focusing at analyte-specific positions. Analyte concentration in the enriched zone approaches a maximum value which is independent of its concentration in the supplying reservoirs. A simple approach is shown to unify the temporal behavior of the concentration factors under general conditions.

Introduction

Multifunctional microchip devices for chemical separation and analysis provide significant advantages in performance, resulting in faster and cheaper analytical procedures by requiring small amounts of sample and reagents. However, the use of smaller geometries also means that the number of molecules to be analyzed is reduced, so that their detection can become a challenging task. Apart from the use of highly sensitive detectors, another option is to employ analyte preconcentration before (off-line) or after (on-line) sample injection. The integration of sample pretreatment into microfluidic devices is one of the remaining hurdles towards achieving true miniaturized total analysis systems.

In the literature, numerous sample preconcentration methods have been reported for miniaturized devices. They include approaches based on electrokinetic equilibrium techniques like field amplified sample stacking,[1–4] temperature gradient focusing,[5–9] isotachophoresis,[10–15] isoelectric focusing,[16–20] conductivity gradient focusing,[21–23] and electric field gradient focusing.[24–28] Other methods utilize specific interactions (*e.g.*, electrostatic, hydrophilic, affinity) between analytes and the surface of the microchannel walls,[29–32] or employ size- and electrostatic-exclusion as well as concentration polarization at nanoporous membranes and discrete nanochannels.[33–48]

Electrofocusing is an accompanying effect of electrophoretic equilibrium gradient methods, a subset of separation techniques in which a net restoring force acts against dispersive forces to simultaneously separate and concentrate. Because most electrofocusing techniques are not generally applicable, the only widely used technique in this family is isoelectric focusing (IEF). IEF is based on the fact that the net charge of molecules becomes zero if the pH of the surrounding solution is equal to the molecules isoelectric point (p*I*). Thus, if a pH gradient exists in the system, analytes can be immobilized and accumulated where pH = p*I*. However, the application of IEF-methods is limited. This technique can only be employed with an analyte having a well-defined p*I*. In addition, the solubility of proteins at their p*I* is low, and that handicaps the application of IEF-methods to biochemical systems.[39]

The scarcity of available electrofocusing-based methods has motivated recent development,[49] especially of techniques which can be applied to microelectromechanical platforms.[50] Recently, we reported a novel electric field gradient focusing technique for use in a straight microchannel device containing an embedded floating (bipolar) gold electrode which, at any time, is no part of the external circuitry.[51] This experimentally simple approach enables analyte enrichment because of the formation of a steep electric field gradient within the (6 mm long, 100 μm wide, and ~20 μm high) microchannel. The floating electrode (500 μm long) in the electrolyte-filled microchannel nearly eliminates the electric field in its vicinity, and a spatially extended field gradient develops in the adjoining anodic compartment. The formation of this field gradient is the consequence of a complex interplay between electrophoretic, bulk convective, and diffusive transport of the background electrolyte ions. The effect of this field gradient has been visualized using negatively charged fluorescent tracer molecules, which experience counter-directional forces of bulk convection and electrophoresis to become quasi-stationary and locally enriched. Transport effects, that can be explained by a very similar mechanism, have been recently reported by Piruska *et al.*[52] in their study of electrokinetic transport within three-dimensional hybrid nanofluidic–microfluidic devices incorporating gold-coated nanocapillary array membranes.

The effect of a floating (bipolar) electrode in the surrounding electrolyte solution has been investigated in some detail recently

---

[a] *Department of Chemistry, Philipps-Universität Marburg, Hans-Meerwein-Strasse, 35032 Marburg, Germany. E-mail: tallarek@staff.uni-marburg.de*
[b] *Department of Chemistry and Biochemistry, Center for Electrochemistry, The University of Texas at Austin, 1 University Station, A5300, Austin, TX, 78712-0165, USA. E-mail: crooks@cm.utexas.edu*

with an emphasis on electrochemical reactions[53–55] and induced-charge electroosmosis.[56–59] For example, Duval and co-workers[53–55] theoretically investigated coupled electrochemical phenomena and mass/charge transport in channels with electron-conducting walls or surfaces. For those systems, it was assumed that gaps between the external electrodes and a conducting wall/surface were infinitely small, and an applied potential bias must completely drop over the electron-conducting region. However, in this paper we will show that the presence of the ion-conducting region between the external and floating electrodes dramatically changes the properties of the system.

Bazant and co-workers[56–58] and also Yariv and Miloh[59] investigated induced-charge electroosmosis, that is, the nonlinear electroosmotic slip that occurs when an applied field acts on the ionic charge it induces around a polarizable surface. These two groups carried out a theoretical analysis of electric and flow velocity fields around cylindrical and spherical conducting surfaces immersed in an electrolyte solution, but it was assumed that no faradaic reactions occur at the solid–liquid interface.

The relationship between complex (diffusive, electrophoretic, and convective) transport of charged species and faradaic electrochemical reactions was not revealed by these studies of inhomogeneous systems. The importance of a coupling between electrokinetic transport and faradaic reactions at the surface of a floating (bipolar) electrode was demonstrated experimentally by Yeung and co-workers.[60] They inserted a platinum wire of 25–50 μm o.d. into 75 μm i.d. fused-silica capillaries filled with a buffer solution and fluorescent analytes. After the application of an electric field to the capillary, a spatially shifting preconcentration of the analytes was observed, which these authors explained by the formation of a dynamic pH gradient (due to faradaic reactions at the platinum wire) and a subsequent local change of the net charge of the analytes (pH-sweeping mechanism).

Besides faradaic reactions, another aspect relevant to electrokinetic systems with floating electrodes is the actual source of electroosmotic flow (EOF). In the aforementioned theoretical studies,[56–59] it was assumed that the only cause of EOF is the interaction of the externally applied electric field with the induced-charge around a conducting body. This idealization naturally results in a strong correlation between the induced-charge and transport characteristics of the system. At the same time, the generation of EOF at the dielectric walls in confined systems is basically independent of the conductor polarization and can become the dominating factor for the local distribution of charged species, electric field strength, and species transport.

In this paper, we provide a complete theoretical description of experimental data we previously reported[51] and employ the results of numerical simulations for their analysis. The developed theoretical model highlights the complex local interplay between electrokinetics, hydrodynamics, and electrochemistry involved in the formation of an extended electric field gradient further illustrated by a fast, scalable concentration enrichment of charged analytes.

Experimental

Microfluidic device and chemicals

The hybrid poly(dimethylsiloxane) (PDMS)/glass microfluidic device (a layout is shown in Fig. 1) and bipolar electrode were fabricated using standard lithographic techniques.[61] The microfluidic channel was made by attaching a PDMS mold containing a microchannel (6 mm long, 100 μm wide, and ~20 μm high) that connects two macroscale cylindrical reservoirs, A and B (referred to as ResA and ResB), of ~2.5 mm diameter to a microscope glass slide by O_2 plasma bonding (60 W, model PDC-32G, Harrick Scientific, Ossining, NY, USA). Before fabricating the microfluidic device, a floating electrode was prepared by depositing 100 nm of Au (no adhesion layer) onto the glass slide. Then, photolithographic and etching methods were used to pattern a single 500 μm × 1000 μm electrode.

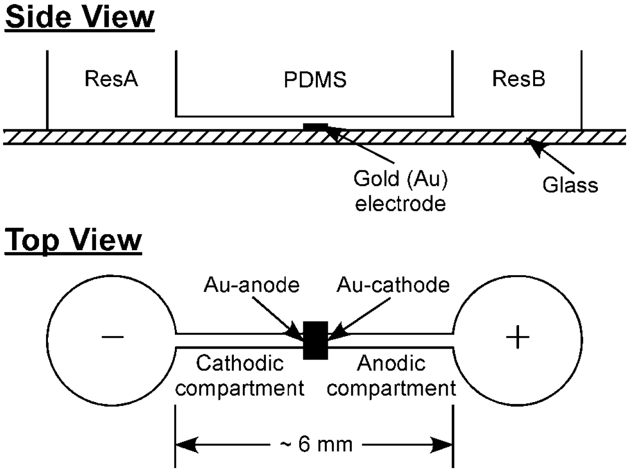

Fig. 1 Layout of the hybrid PDMS/glass microfluidic device. The Au electrode (500 μm × 1000 μm) is at the center of the (6 mm long, 100 μm wide, and ~20 μm high) microchannel connecting the two macroscale cylindrical reservoirs (~2.5 mm in diameter), ResA and ResB.

The silicone elastomer and curing agent (Sylgard 184) used to prepare the PDMS microfluidic devices were obtained from K. R. Anderson, Inc. (Morgan Hill, CA, USA). Molecular biology grade 1 M Tris–HCl buffer (Fisher Biotech, Fair Lawn, NJ, USA) was diluted to 1 mM (pH 8.1) with deionized water (18 MΩ cm, Milli-Q® Gradient System, Millipore) and used as background electrolyte in all experiments. The twice negatively charged BODIPY disulfonate (Molecular Probes, Eugene, OR, USA) was used as fluorescent tracer.

Data acquisition

Prior to each experiment, the microchannel was rinsed by filling ResA with 1 mM Tris–HCl buffer (pH 8.1) and applying a vacuum at ResB for 2 min. Following the rinsing process, the microchannel and reservoirs were filled with 5 μM of BODIPY disulfonate in the same buffer. A 30 V bias was then applied between two platinum electrodes immersed in ResA (grounded; cathode) and ResB (at a positive potential; anode) to generate an electric field within the channel. The average electric field along the channel was estimated to be ~5.0 kV m^{-1}.

Electrokinetic transport of the dye was captured using an inverted epifluorescence microscope (Eclipse TE 2000-U, Nikon, Japan) fitted with a CCD camera (Cascade 512B, Photometrics, Tuscon, AZ, USA). Values of the maximum concentration factor were determined by measuring the width-averaged fluorescence perpendicular to the channel axis as a function of distance along the axis, and then dividing the maximum intensity by the average fluorescence intensity obtained from a reference channel containing a solution of the same dye with the corresponding concentration. All fluorescence measurements were corrected by subtracting the background count.

Analysis of experimental data

Due to contact with the Tris–HCl buffer, the surface of the glass and PDMS walls of the channel acquire negative electric charge. Therefore the generated EOF is cathodic, *i.e.*, the motion of the liquid is directed to the cathode (to ResA in Fig. 1). Since the electrophoretic mobility of the BODIPY disulfonate molecules is less than the bulk electroosmotic mobility, the tracer moves with the EOF from ResB to ResA in the absence of the floating electrode.[51] In contrast, the dye is concentrated to the right of the electrode, in the anodic segment of the channel, if the floating electrode is embedded into the microchannel (Fig. 2). This accumulation of the negatively charged analyte indicates that its transport by the EOF in the system with the floating electrode is locally offset by counter-directional electrophoretic motion.

When the initial concentration of BODIPY disulfonate (c_0) was 5 μM, its concentration in the enriched zone asymptotically tended, with time, to some specific value and did not change after approximately 425 seconds (Fig. 2). In contrast, for the lower initial concentration $c_0 = 0.1$ μM, the dye concentration in the enriched zone continued to grow almost linearly with time.

The data in Fig. 2 cannot be attributed to the pH-sweeping mechanism proposed by Yeung and co-workers.[60] In that case, a dynamic pH gradient was thought to form along the length of the capillary due to faradaic reactions at the embedded platinum-wire bipolar electrode. This pH gradient was proposed to affect the charge on the tracer molecules. The tracers used in their study (fluorescein derivates) had a p*K* close to the pH of the background electrolyte solution and quickly changed their net charge according to the dynamic pH profile.[60] Thus, the point where the electroosmotic force was balanced by the electrophoretic force moved along the channel with the pH gradient. In contrast to that study, we used BODIPY disulfonate, which is strongly acidic and has a p*K* of about 2,[62] which is far from the Tris buffer pH of 8.1. This means that the concentration enrichment in our studies cannot be dominated by a pH gradient. To quantitatively interpret the results, in Fig. 2 we have developed a theoretical model of relevant physicochemical processes occurring in this device, including buffer and faradaic reactions, and carried out numerical simulations.

Theoretical background and mathematical model

Spatiotemporal variations in the concentrations of ionic species of the buffer solution and the tracer molecules in the studied system are governed by balance equations

$$\frac{\partial c_i}{\partial t} = \nabla(D_i \nabla c_i) - \frac{z_i F}{RT}\nabla(D_i \nabla \phi) - c_i \nabla \boldsymbol{v} + r_i \qquad (1)$$

where c_i is the molar concentration of species *i*, D_i and z_i are its diffusion coefficient and valency, respectively, ϕ is the local electric potential; *F*, *R* and *T* represent the Faraday constant, molar gas constant and temperature, respectively, $\boldsymbol{v}$ is the flow velocity, and r_i is the homogeneous reaction term for species *i*. We assume that the diffusion coefficient of the species is not affected by their local concentration.

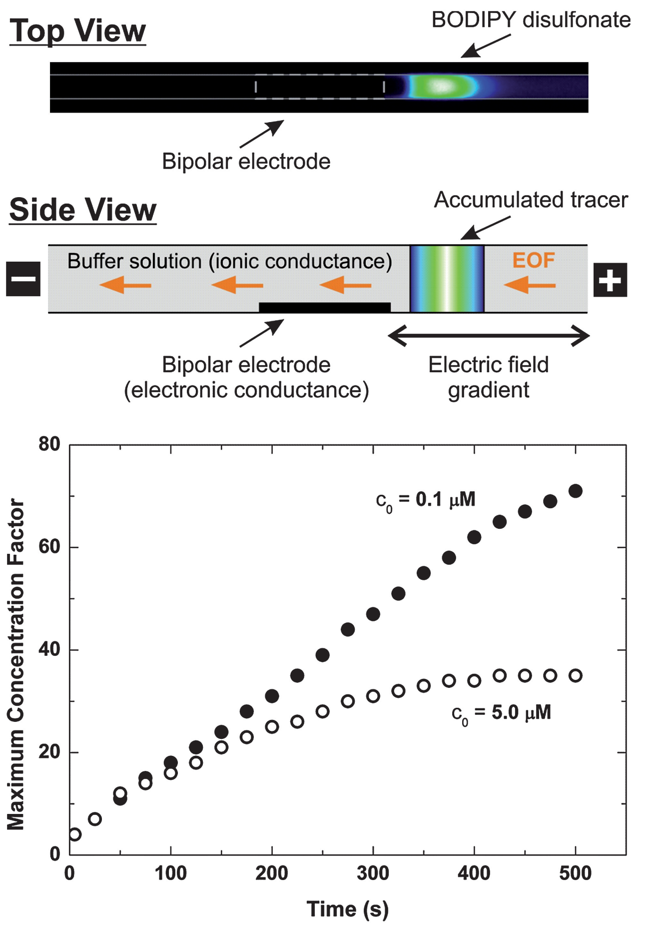

Fig. 2 Optical fluorescence micrograph of the microchannel with the embedded Au electrode. The micrograph shows the concentration distribution of BODIPY disulfonate in 1 mM Tris–HCl buffer at pH 8.1 after applying a potential bias of 30 V for 240 s (top). Schematic illustration of the proposed mechanism of tracer accumulation in the microchannel with a bipolar electrode (middle). Maximum concentration factor in the enriched zones experimentally measured for different initial concentrations of BODIPY disulfonate in 1 mM Tris–HCl buffer at pH 8.1 with an applied potential bias of 30 V as a function of time (bottom).

The local concentrations of the charged species and the local electric potential are related by the Poisson equation

$$\nabla^2 \phi = -\frac{F}{\varepsilon_0 \varepsilon_r}\sum_i z_i c_i \qquad (2)$$

where ε_0 and ε_r are the vacuum permittivity and dielectric constant, respectively. Assuming that the liquid is incompressible, the generalized Navier–Stokes equation establishes the relation between the local flow velocity, pressure, and the electric body force

$$\rho\left(\frac{\partial \boldsymbol{v}}{\partial t} + \boldsymbol{v} \cdot \nabla \boldsymbol{v}\right) = -\nabla p + \mu \nabla^2 \boldsymbol{v} - (\nabla \phi)\sum_i z_i c_i \qquad (3)$$

where ρ and μ are the mass density and dynamic viscosity of the liquid, and *p* is the hydrostatic pressure.

The numerical solution of the coupled eqn (1)–(3) is a non trivial task, as it has to be accomplished at different spatiotemporal scales ranging from the order of the electric double layer thickness of typically 1–10 nm, to the length of the channel of several millimetres. These widely disparate spatial scales require huge computational resources. One possibility to avoid this limitation is to assume that the electric double layer thickness is negligibly small compared with the channel dimensions (thin-double layer approximation).[63] The studied system meets the above requirement as the electric double layer thickness is ~10 nm in the presence of 1 mM Tris buffer. With the thin-double layer approximation, the no-slip condition at the solid–liquid interface for the fluid flow is replaced by the velocity boundary condition formulated according to the Helmholtz–Smoluchowski equation. In this picture, the EOF slips past the solid-liquid interface. Finally, we assume that the geometry can be reduced to a two-dimensional configuration, where the width of the channel is infinite and all parameters vary only along the x- and y-axes.

The two-dimensional geometry of the simulated device is shown in Fig. 3. It is assumed that the microchannel is terminated by two relatively large reservoirs containing the electrodes—ResA with the cathode and ResB with the anode. Eqn (1) and (2) were complemented by the corresponding boundary conditions: for the species balance equation (eqn (1)), we specify zero flux across the channel walls and constant species concentrations at the left and right edges of the channel; for the Poisson equation (eqn (2)), fixed potentials are assumed at the left and right edges of the channel, while at the solid-liquid interface the following boundary conditions were imposed

$$E^{\parallel}_{\text{liquid}} = E^{\parallel}_{\text{solid}} \text{ and } \varepsilon_{\text{liquid}} E^{\perp}_{\text{solid}} = \varepsilon_{\text{solid}} E^{\perp}_{\text{liquid}} \tag{4}$$

where $\parallel$ and $\perp$ denote the tangential and normal components of the local electric field, respectively. In this study the dielectric constants of the aqueous electrolyte solution and the channel walls are assumed to be 80 and 3, respectively.

In order to represent the floating (bipolar) electrode, we used the electron gas model.[64] According to this approach, valence electrons of the atoms comprising a metal are able to leave them and move through the whole electrode accounting for electrostatic interactions. Thus, the metal electrode is assumed to be composed of two kinds of interacting charges: mobile negatively charged (electron gas; however, it is not allowed to leave the electrode) and immobile positively charged species (ions of the lattice). In the absence of an external electric field, the whole electrode is electrically neutral because of the presence of the same amount of both kinds of charges. In addition, the volume density of the electron gas is uniform throughout the electrode. If an external electric field is applied to the metal–"environment" interface, electrons are redistributed to compensate this external distortion and form an electrostatic shield, restraining their further electromigration within the electrode. In turn, this leads to the formation of two regions with local non-zero volume charge density at the two opposite sides of the electrode. The side towards ResA (to the external cathode) is characterized by a depletion of electrons. Therefore, it can be considered as an electron sink for faradaic reactions or as an "induced anode". The opposite side of the bipolar electrode, towards ResB (to the external anode), can be considered as an "induced cathode" because of an excess of electrons in this region. The bipolar electrode is represented as a region impermeable to the ions of the electrolyte solution and is characterized by extremely high average concentrations of the mobile and immobile charges (10^6 times higher than the ionic concentration of the background electrolyte solution).

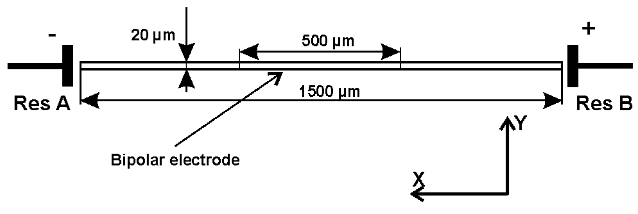

Fig. 3 Illustration of the 2D system used in the simulations for analyzing tracer concentration enrichment in a microfluidic device containing a flat bipolar electrode (*cf.* Fig. 1). This electrode is attached locally to the bottom wall from $x = 500$–1000 µm and has a thickness (in the y-direction) of 3 µm.

Initially, the microchannel and reservoirs are assumed to be filled with 5 µM BODIPY disulfonate in 1 mM Tris–HCl buffer (pH 8.1). Thus, the species of interest include neutral Tris, its protonated form (TrisH^+), hydroxide and hydronium ions (OH^- and H_3O^+), and the tracer molecules (BODIPY disulfonate, twice negatively charged). If no external electric field is applied along the microchannel, water protolysis

$$2H_2O \leftrightarrow H_3O^+ + OH^- \tag{5}$$

and the buffer reaction

$$\text{Tris} + H_2O \leftrightarrow \text{TrisH}^+ + OH^- \tag{6}$$

result in the following uniform (initial) species concentrations in the system:

$$[H_3O^+] = 10^{-\text{pH}} = 7.943 \times 10^{-6} \text{ mM}$$

$$[OH^-] = 10^{(\text{pH}-14)} = 1.259 \times 10^{-3} \text{ mM}$$

$$[\text{Tris}] = 0.515 \text{ mM}$$

$$[\text{TrisH}^+] = [\text{Cl}^-] = 0.485 \text{ mM}$$

The reaction terms in eqn (1) for each species can be represented as

$$r_{H_3O^+} = \frac{\partial[H_3O^+]}{\partial t} = k_1[H_2O] - k_{-1}[H_3O^+][OH^-]$$

$$r_{OH^-} = \frac{\partial[OH^-]}{\partial t} = k_1[H_2O] - k_{-1}[H_3O^+][OH^-] + k_2[\text{Tris}] - k_{-2}[\text{TrisH}^+][OH^-]$$

$$r_{\text{TrisH}^+} = \frac{\partial[\text{TrisH}^+]}{\partial t} = k_2[\text{Tris}] - k_{-2}[\text{TrisH}^+][OH^-]$$

$$r_{\text{Tris}} = \frac{\partial[\text{Tris}]}{\partial t} = -k_2[\text{Tris}] + k_{-2}[\text{TrisH}^+][OH^-]$$

$$r_{\mathrm{Tracer}^{2-}} = \frac{\partial[\mathrm{Tracer}^{2-}]}{\partial t} = 0$$

where k_1 and k_{-1} denote the rate constants for the forward and backward reaction of water self-ionization (eqn (5)), while k_2 and k_{-2} are the rate constants for the forward and backward buffer reaction (eqn (6)).

Apart from the bulk reactions (eqn (5) and eqn (6)), the local species concentrations can change due to faradaic reactions on the surface of the electrodes. One can show that a system with a single floating electrode exposed to an electrolyte solution in a microchannel behaves as two series-connected complete electrochemical cells.[65] Typical electrode reactions for an aqueous solution involve anodic oxygen and cathodic hydrogen evolution, and the concomitant production of H_3O^+ and OH^- due to protolysis of water.

In any aqueous alkaline solution, the oxygen evolution reaction commences on the basis of hydroxide ion oxidation

$$4OH^- - 4e^- \rightarrow O_2 + 2H_2O \tag{7}$$

which shows a diffusion limitation,[66–69] as the supply of OH^- is rate limiting. Due to the deficiency of hydroxide ions, the protolysis equilibrium of water

$$8H_2O \leftrightarrow 4H_3O^+ + 4OH^- \tag{8}$$

is shifted and the concentration of hydronium ions increases nearby the anode. Thus, the final balance is in terms of protolysis theory

$$\begin{gathered} 6H_2O - 4e^- \leftrightarrow O_2 + 4H_3O^+, \text{ or} \\ 2H_2O - 4e^- \leftrightarrow O_2 + 4H^+ \end{gathered} \tag{9}$$

in terms of electrolytic dissociation theory. It should be mentioned that, in addition to the hydroxide ions, chloride ions can also be discharged on the anode

$$2Cl^- - 2e^- \rightarrow Cl_2 \tag{10}$$

The reaction on the cathode is

$$2H_3O^+ + 2e^- \rightarrow H_2 + 2H_2O \tag{11}$$

Due to the deficiency of hydronium ions, the protolysis equilibrium of water

$$4H_2O \leftrightarrow 2H_3O^+ + 2OH^- \tag{12}$$

is shifted and the concentration of hydroxide ions increases nearby the cathode. Thus, the final balance is

$$2H_2O + 2e^- \leftrightarrow H_2 + 2OH^- \tag{13}$$

On the cathode, along with the above-described reaction of the hydrogen evolution, reduction of $TrisH^+$ can also take place

$$2TrisH^+ + 2e^- \rightarrow H_2 + 2Tris \tag{14}$$

Thus, the model includes electrochemical reactions described by eqn (9), eqn (10), eqn (13) and eqn (14), which take place at the right (induced cathode) and left (induced anode) faces of the bipolar electrode. We assume that the rates of the faradaic reactions are much higher than those of the chemical reactions (eqn (5) and eqn (6)). This assumption is recognized in the model as complete "consumption" of the corresponding ions in direct vicinity of the bipolar electrode due to the faradaic reactions. It should be noted that faradaic reactions can also take place at the anodic and cathodic electrodes in ResA and ResB. However, most of the applied potential is dropped in the channel and the volume of the reservoirs is large compared to the channel, so the impact of electrolysis in the reservoirs should be small. Therefore, in our mathematical model, we assume that species concentrations in ResA and ResB are constant.

Table 1 Species properties considered in the simulations

Species	Diffusion coefficient	Charge
Tris	0.785×10^{-9} m^2 s^{-1}	0
$TrisH^+$	0.785×10^{-9} m^2 s^{-1}	+1
Cl^-	2.033×10^{-9} m^2 s^{-1}	−1
H_3O^+	5.286×10^{-9} m^2 s^{-1}	+1
OH^-	5.286×10^{-9} m^2 s^{-1}	−1
Tracer molecules	0.427×10^{-9} m^2 s^{-1}	−2

Table 2 Reaction rate constants for eqn (5) and (6)

k_1 (eqn (5), forward)	2×10^{-5} s^{-1}
k_{-1} (eqn (5), backward)	1.11×10^{8} m^3 mol^{-1} s^{-1}
k_2 (eqn (6), forward)	2×10^{-6} s^{-1}
k_{-2} (eqn (6), backward)	1.11×10^{7} m^3 mol^{-1} s^{-1}

The mathematical description of the processes in the studied system was implemented as an iterative model based on discrete spatiotemporal schemes optimized for parallel computations. In particular, for the solution of the Navier–Stokes, Poisson and Nernst–Planck equations, respectively, the lattice-Boltzmann approach[70] and the numerical approaches proposed by Warren[71] and by Capuani *et al.*[72] were employed. In all numerical schemes, a time step of 2×10^{-5} s and a space step of 10^{-6} m were used. At each time step, the Poisson equation was solved 10 times with an under-relaxation factor of 0.25 in order to ensure numerical stability. A single simulation required about 16 h at 64 processors of an SGI Altix 4700 supercomputer to analyze the temporal behavior of the system for 500 s. Physicochemical parameters used in the simulations are given in Tables 1 and 2.

Results and discussion

To correspond as closely as possible with experimental data, the complete microchannel and both reservoirs in the simulated system (Fig. 3) were assumed to be filled uniformly with the tracer in 1 mM Tris–HCl buffer (pH 8.1) at an initial concentration of $c_0 = 5$ μM. Then, a bias of 7.5 V ($E = 5$ kV m^{-1}) was applied to the channel and the evolution of two-dimensional distributions of electric potential and species concentrations was recorded every 2 s. We assume that the electrokinetic potential at the microchannel wall is −50 mV. This magnitude is typical for PDMS surfaces, taking further into account the actual pH and ionic strength of the electrolyte solution.[73]

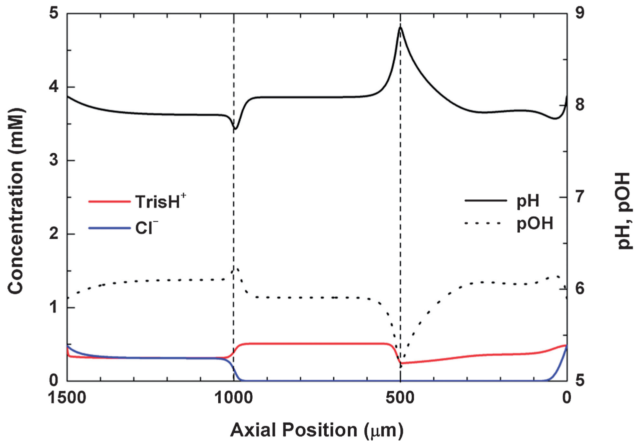

Fig. 4 Simulated profiles of the background ion concentrations (in mM), and pH and pOH for $t = 200$ s. Applied field strength: 5 kV m^{-1}. Initial tracer concentration, $c_0 = 5$ μM. Profiles represent the distribution along the geometrical axis of the channel ($y = 10$ μm). The bipolar electrode is located at the wall from $x = 500$–1000 μm.

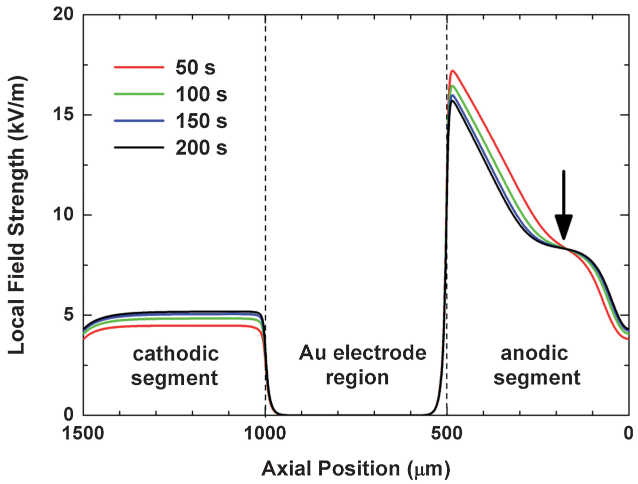

Fig. 5 Simulated profiles of the local axial electric field for $t = 50$, 100, 150, and 200 s. Applied field strength: 5 kV m^{-1}. Initial tracer concentration, $c_0 = 5$ μM. Profiles represent the distribution of field strength along the geometrical axis of the channel ($y = 10$ μm).

The data simulated under these conditions demonstrate a close correlation between local species concentrations (Fig. 4) and local electric field strength along the microchannel (Fig. 5). Nonuniform species concentration distributions can be understood in terms of the nonuniformity of the local electric field and, as a result, differences in local transport rates of individual species. In Fig. 4, bulk convection originating in the EOF is from the right to the left, also above the electrode. This has important consequences for electrophoretic transport of charged species: they accelerate or decelerate depending on the local field strength. For cations, the electroosmotic and electrophoretic flux components are co-directional (from ResB to ResA), and, hence, their sum is proportional to the local field strength. Because field strengths in the anodic and cathodic microchannel segments and in the region above the bipolar electrode are related by $E_{\text{anode}} > E_{\text{cathode}} > E_{\text{bipolar}}$, steady-state concentrations of cations in these regions must correspond to $c_{\text{bipolar}} > c_{\text{cathode}} > c_{\text{anode}}$ in order to conserve charge flux. For anions, these fluxes due to electroosmotic flow and electrophoresis are counter-directional and their sum decreases as the local field strength increases, and even becomes negative in the anodic segment (*i.e.*, net transport is directed from ResA to ResB).

Specifically, the chloride ions in the anodic microchannel segment ($x < 500$ μm, Fig. 4) move towards the right (to the anode), because their electrophoretic mobility is decidedly higher than the general EOF mobility in the system. In what follows, it is most important that their local withdrawal cannot be supplied by other chloride ions which would be positioned at $x > 500$ μm. In the neighboring microchannel compartment ($500 < x < 1000$ μm), which contains the bipolar electrode along the bottom wall (*cf.* Fig. 3), the electric field strength becomes zero (Fig. 5). Thus, electrophoretic motion of chloride ions is not possible in this bipolar electrode segment, where charge transport in the liquid phase is dominated by bulk convection through the microchannel from right to left. As a consequence, there are no chloride ions above the bipolar electrode that could compensate the local withdrawal of chloride ions in the anodic microchannel compartment which here ($x < 500$ μm), due to their dominating electrophoretic motion and strong local field strengths up to 15–17 kV m^{-1} (with respect to the applied 5 kV m^{-1}, Fig. 5), move towards the external anode. This depletion region stops where (along this extended field gradient, towards $x = 0$ μm) electrophoretic and electroosmotic contributions for the chloride ions compensate each other (for $x < 50$ μm in Fig. 4 and 5, local field strength here drops below 5 kV m^{-1}).

For the TrisH$^+$ ions (Fig. 4) there is an increased concentration in the region $x \approx 500$–1000 μm. This is caused by bulk convection, which dominates charge transport above the bipolar electrode, while in the cathodic compartment ($x = 1000$–1500 μm) TrisH$^+$ ions experience (co-directional) flow and electrophoresis to the left electrode (cathode). As noted earlier, in order to conserve the charge flux throughout the interconnected system, the lower transport rate above the bipolar electrode is compensated by a higher concentration. The concentration profile of the TrisH$^+$ ions in the anodic compartment stems from their buffer reaction with the OH$^-$ ions, which are produced at the cathode of the bipolar electrodes ($x = 500$ μm) and swept towards the external anode. Thus, the concentration of TrisH$^+$ ions in the anodic microchannel compartment is reduced, mostly at/close to the bipolar electrodes cathode ($x = 500$ μm), and then recovers towards the anodic reservoir.

Since the local electric field strength is inversely proportional to the conductivity, the significantly reduced and nonuniform concentration of background electrolyte ions in the anodic segment leads to the formation of an extended electric field gradient, with field strength increasing from the external anode (ResB) to the right edge of the bipolar electrode (Fig. 5). This is the key to understanding this device in view of analyte concentration enrichment: the extended field gradient forms due to the presence of the EOF and the bipolar electrode, which "divides" the microchannel into three segments with different transport characteristics. We have seen in complementary simulations that without the EOF an extended field gradient, as in Fig. 5 (which covers the complete anodic microchannel segment), is not formed. The field gradient is then limited to the rapid drop in field strength close to the boundaries of the bipolar electrode segment (around $x = 500$ and 1000 μm) also seen in Fig. 5.

Fig. 4 shows that in regions close to the edges of the bipolar electrode ($x = 500$ and 1000 μm) the concentrations of hydronium and hydroxide ions (pH, pOH) change more significantly than those of the background electrolyte ions ($\mathrm{TrisH^+}$, $\mathrm{Cl^-}$). This is a clear result of the faradaic reactions which occur at both edges of the electrode. In contrast to the background electrolyte ions, the concentrations of hydronium and hydroxide ions are balanced also by the buffer reaction and water dissociation; therefore, they "restore" their equilibrium concentrations relatively rapidly in these critical regions close to the electrode.

It should be mentioned that the application of the external electric field leads to a redistribution of the electrons within the bipolar electrode: there is an excess of electrons at the right edge of the electrode ("bipolar electrodes cathode"), while its left edge ("bipolar electrodes anode") is characterized by a reduced concentration of electrons. Fig. 6 enables a two-dimensional analysis of the local electric field in the important regions very close to the edges of the bipolar electrode. Just to recall, the bipolar electrode in the simulations is 3 μm thick and covers the microchannel bottom wall at $x = 500$–1000 μm (*cf.* Fig. 3). The direction of the arrows in Fig. 6 indicates the orientation of a local field line, while the length of the arrows corresponds to the field strength at this point. It is seen that in most of the anodic and cathodic compartments, field lines are parallel to the channel walls and the electric field contains exclusively the axial component. However, the field lines become warped at distances below 5 μm from the edges of the electrode: the bipolar electrodes cathode ($x = 500$ μm) "collects" the field lines, while the induced anode ($x = 1000$ μm) acts as their "source". Above the electrode, the axial component of the electric field exists only within a small region (~5 μm) close to both edges.

The implication of the nonuniform distribution of the local electric field along the microchannel (Fig. 5 and 6) is that tracer molecules, which come from the anodic reservoir due to the initially (more precisely, locally) dominant bulk convection based on the EOF, encounter an increasing electrophoretic force in the opposite direction (that is, back towards ResB) as they approach the bipolar electrode. This is illustrated by Fig. 7, which shows how the local electroosmotic ($\boldsymbol{v}_{\mathrm{eo}}$) and

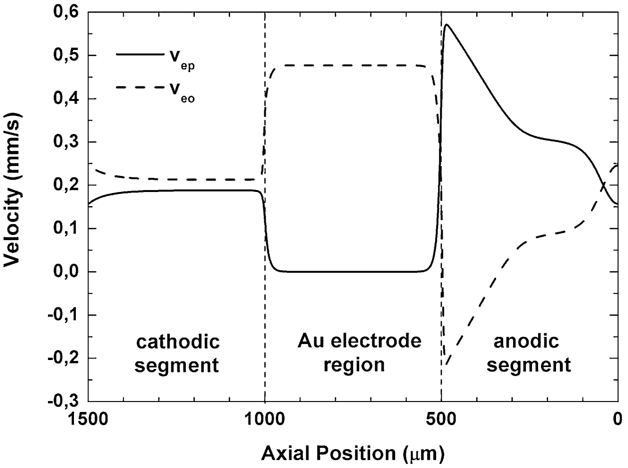

Fig. 7 Simulated profiles of local electrophoretic ($\boldsymbol{v}_{\mathrm{ep}}$) and electroosmotic ($\boldsymbol{v}_{\mathrm{eo}}$) velocities of the tracer for $t = 200$ s. Applied field strength: 5 kV $\mathrm{m^{-1}}$. Initial tracer concentration, $c_0 = 5$ μM. Profiles represent the distribution of velocities along the geometrical axis of the channel ($y = 10$ μm).

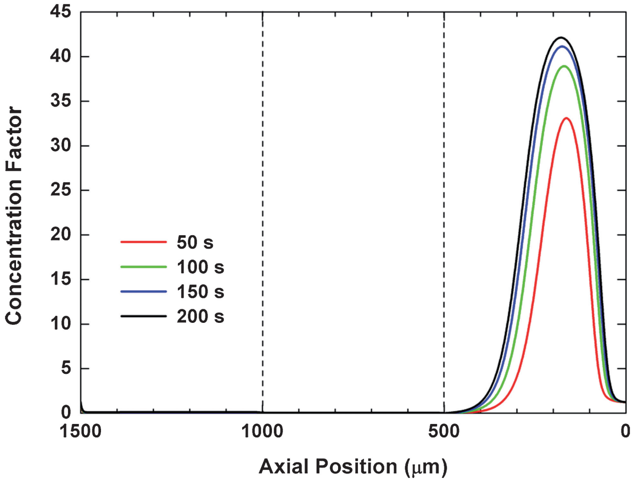

Fig. 8 Simulated tracer concentration profiles for $t = 50$, 100, 150, and 200 s. Applied field strength: 5 kV $\mathrm{m^{-1}}$. Initial tracer concentration, $c_0 = 5$ μM. Profiles represent the distribution of the concentration factor along the geometrical axis of the channel ($y = 10$ μm).

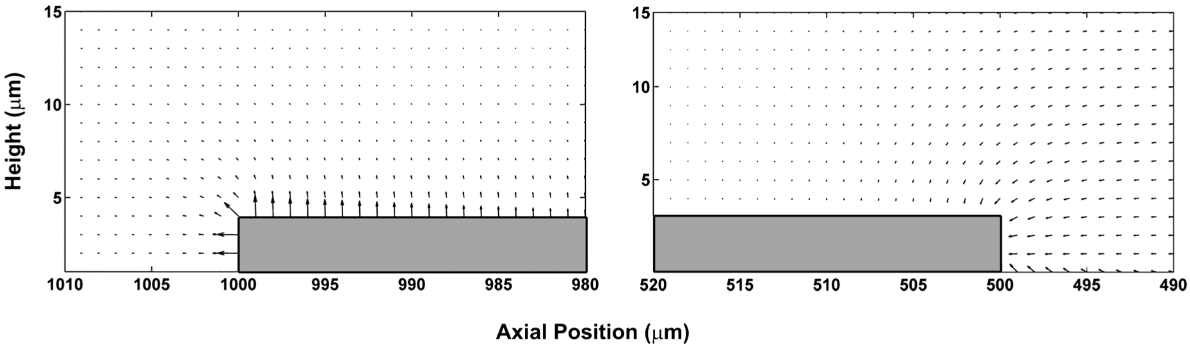

Fig. 6 Close-up views of the local electric field adjacent to the edges of the bipolar electrode at $x = 500$ and 1000 μm for $t = 200$ s. The direction of arrows represents the orientation of a field line, while their length corresponds to the local field strength. Horizontal and vertical axes indicate the position (in μm) along x- and y-directions in the microchannel (*cf.* Fig. 3).

electrophoretic ($\boldsymbol{v}_{ep}$) velocities of the tracer molecules change with their axial position. The nonuniform distribution of the EOF velocity along the microchannel (shown in Fig. 7 for its geometrical axis, $y = 10$ μm) is a direct result of local pressure gradients which develop as a consequence of a nonuniform electrokinetic body force. In particular, in the segment containing the Au electrode, where the electric field drops to zero, there will be no electroosmotic force and the flow will be pressure-driven. As a result, convex or concave velocity profiles form in the different segments of the microchannel, and local flow recirculation near the bipolar electrode (segment boundaries) even leads to negative velocity components. Fig. 7 also provides a means to compare the absolute values of $\boldsymbol{v}_{ep}(x)$ with $\boldsymbol{v}_{eo}(x)$ for $t = 200$ s: at a certain axial position (here at $x \approx 50$ μm, but depending on the elapsed time and y-position), the two counter-directional motions (*i.e.*, anodic electrophoresis *vs.* cathodic electroosmosis) are balanced; tracer molecules become quasi-stationary and locally enriched (Fig. 8).

The step-like character of the field strength profile in the anodic microchannel segment (see arrow in Fig. 5) can be explained by the concentration enrichment history of the negatively charged tracer shown in Fig. 8. The actual tracer concentration becomes comparable with the background ion concentration (1 mM Tris–HCl buffer solution). As a consequence, the local field strength is a function of the tracer concentration as well as that of the buffer. Following its increase with time, the interplay of fluxes due to bulk convection, electrophoresis, and diffusion results in a broadening of the developing tracer zone. The axial position and the width of this zone at any time (Fig. 8) exactly correspond to those of the "steps" (plateaus) in the field strength profiles indicated by the arrow in Fig. 5.

The influence of the actual ionic concentration in the enriched tracer zone on the local field strength is further illustrated by Fig. 9. It presents simulated profiles of electric field strength for different initial tracer concentrations, $c_0 = 5$ μM and 5 nM. After 200 s the highest concentrations in the enriched tracer zones were 0.202 mM and 3.781 μM, respectively. The latter concentration is still much lower than that of the background electrolyte, while the former is already comparable with it. Therefore, the electric field strength profile for $c_0 = 5$ nM after $t = 200$ s does not show any signs of the plateau, but is still characterized by a nearly constant field gradient in the anodic microchannel compartment (which reflects the situation without tracer in the system).

Another conclusion from these results can be reached, if one determines the maximum concentration factor as the ratio of the highest concentration in the enriched zone to the initial tracer concentration, these ratios (after $t = 200$ s) are 42.1 and 753 for $c_0 = 5$ μM and 5 nM, respectively; then, a simple reduction of the initial concentration results in a much higher concentration enrichment factor. We performed simulations for further initial tracer concentrations ($c_0 = 0.1$, 0.5, 1.0, and 2 μM) and analyzed maximum concentration factors. The results in Fig. 10 indicate that maximum concentration factors develop similarly and asymptotically tend to some specific value, just on different time

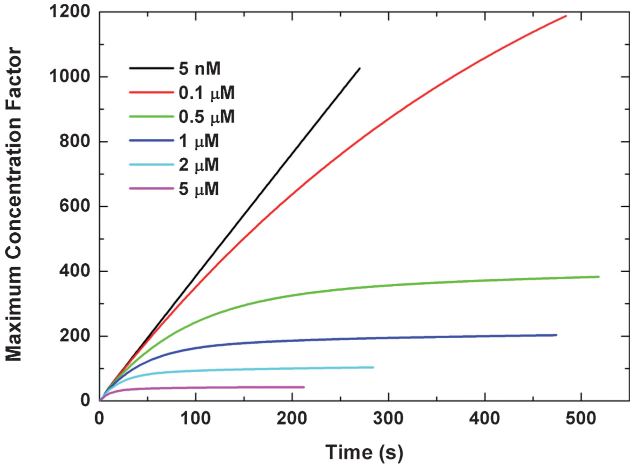

Fig. 10 Simulated maximum concentration factors *versus* time for different initial tracer concentrations, as indicated. Applied field strength: 5 kV m^{-1}.

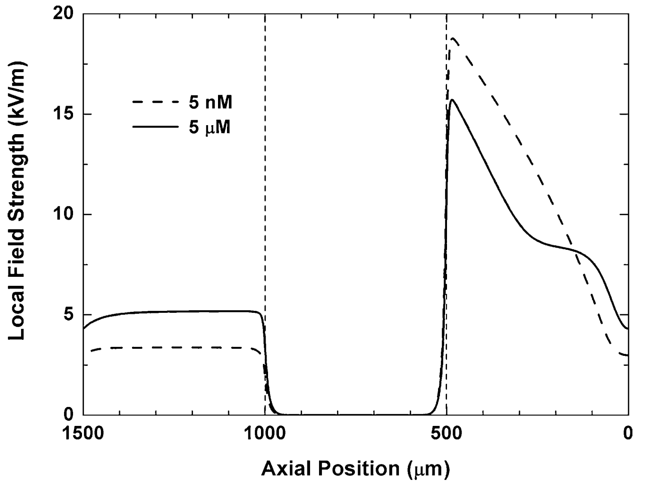

Fig. 9 Simulated profiles of the local axial electric field after $t = 200$ s with 5 nM and 5 μM initial tracer concentration. Applied field strength: 5 kV m^{-1}. Profiles represent the distribution of field strength along the geometrical axis of the channel ($y = 10$ μm).

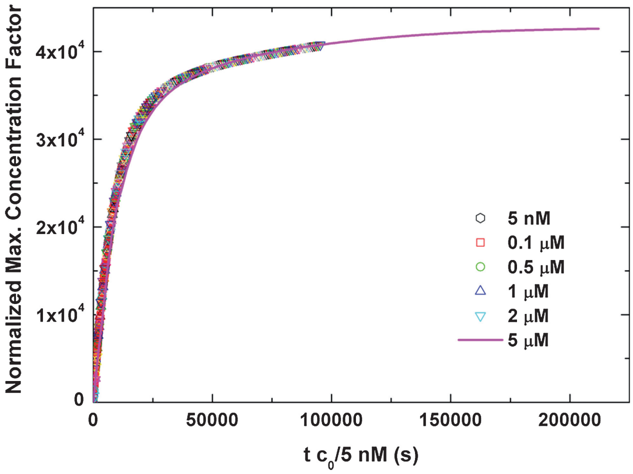

Fig. 11 Normalized maximum concentration factors *versus* time for different initial tracer concentrations. Applied field strength: 5 kV m^{-1}. Maximum concentration and times corresponding to each initial tracer concentration (c_0) were scaled by multiplication with the factor c_0/(5 nM).

scales. We attempted to unify these data in Fig. 10 by an expansion of the time- and maximum concentration factor-axes, using the ratio of the corresponding initial tracer concentration (c_0) to the smallest one (c_0 = 5 nM). As seen in Fig. 11, the normalized curves collapse nearly perfectly. It demonstrates that the temporal behavior of the maximum concentration factor for any initial tracer concentration could be estimated using a single data set, representing the development of the maximum concentration factor for a single initial concentration. The temporal behavior of the maximum concentration factor for a different value of c_0 can then be obtained by correcting the original data set just by a numerical factor.

It should be pointed out that a quantitative comparison between the experimental data and the simulation results is impeded by a number of factors which are not included in the current model. While Fig. 11 demonstrates perfect scaling of maximum concentration factors with time and initial concentration based on the simulations, deviations from this ideal behavior in practice (Fig. 2) may be related to changes in average velocity and flow profiles, and/or the intensity of faradaic reactions, particularly during the longer times required for sweeping large amounts of sample containing the species of interest in most dilute form. In addition, these deviations can be a result of the difference in the microchannel inlet boundary conditions. In our simulations, we assume that species concentrations at the microchannel inlet (in the anodic reservoir) are constant, equal to the initial ones and do not change with time. However, the actual spatiotemporal distribution of species concentrations in the reservoirs is more complicated. The dominating transport mechanisms for the charged analyte molecules in the reservoirs are diffusion and electrophoresis. Thus, the application of the potential bias forces the negatively charged species (including the analyte molecules) in the anodic reservoir to migrate towards the anode. This redistribution can result in the formation of a diluted zone (as compared to the initial concentration in the reservoir) nearby the microchannel inlet and, as a consequence, in a reduced amount of tracer molecules entering the microchannel. This can explain why experimentally observed enrichment factors increase slower with time than in the simulations. Thus, a side-by-side comparison between experiments and simulations requires that the macroscale reservoirs A and B be included in the simulated system. In the present study we could not realize this due to restrictions in computational resources.

One more conclusion from the data in Fig. 11 is that the tracer concentration in the enriched zone tends towards the same absolute value regardless of its initial concentration in the system. This conclusion is supported by the data in Fig. 12, which show the increase of tracer concentration in the enriched zone with time for all different initial concentrations. Even though in our simulations we did not reach the associated stationary regimes due to restrictions in computational times, it appears that the data in Fig. 12 demonstrate a unique behavior by approaching the same asymptotic value. This can be understood by the local interplay between ionic strength due to the enriched tracer and electric potential drop which, with respect to a given ionic strength of the background electrolyte, starts becoming significant at a certain absolute tracer concentration, resulting in a degradation of the field gradient with "locally flat" field strength profile (see arrow in Fig. 5).

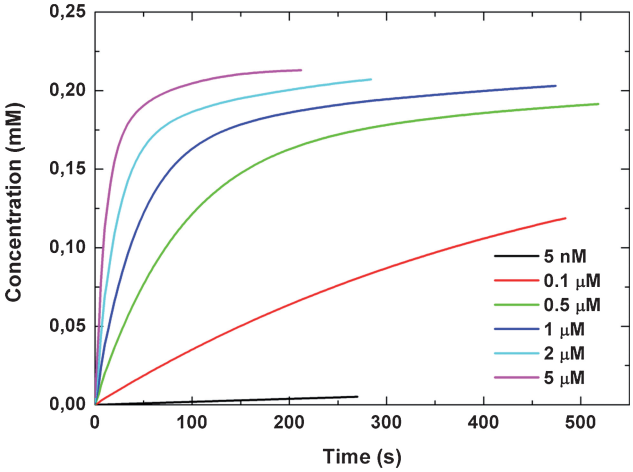

Fig. 12 Simulated highest concentration in the enriched tracer zone *versus* time for different initial concentrations, as indicated. Applied field strength: 5 kV m^{-1}.

All these results show that a maximum concentration factor alone is not adequate to characterize comprehensively the efficiency and actual performance of a preconcentration device. For example, the data in Fig. 10 and 11 indicate that the investigated device allows to achieve optionally a maximum concentration factor of 42.1 with $c_0 = 5$ μM, 421 ($c_0 = 0.5$ μM), or 4.21 × 10^4 (c_0 = 5 nM). Thus, a simple manipulation of the initial tracer concentration leads to quantitatively and qualitatively different ratings of the device. In our opinion, it will then be necessary to analyze, at least, two additional parameters (apart from the maximum concentration factor) for the characterization of preconcentration, namely the initial analyte concentration and the actual rate (required time) for achieving the maximum concentration factor.

Conclusions

We have used detailed numerical simulations to analyze an electric field gradient focusing mechanism in view of analyte concentration enrichment recently observed in a hybrid PDMS/glass straight microchannel containing a floating (bipolar) electrode. The unique properties of the embedded electrode due to its electronic conductance, which contrasts with the much lower ionic conductance of the surrounding electrolyte solution, result in a redistribution of the local field strength along the microchannel after the application of an external electric field. Together with bulk convection of liquid through the whole microchannel based on cathodic EOF, an extended field gradient is formed in the anodic microchannel compartment of the device between external anode and the bipolar electrodes cathode. It imparts a spatially dependent electrophoretic force on charged analytes and, in combination with the bulk convection, results in their focusing at analyte-specific positions. The accumulation of charged analytes in a specific region of the system is a result of zero net driving force, considered as the sum of electrophoretic and convective components. The accompanying faradaic and buffer reactions, as well as water auto-dissociation, can further affect the local species concentrations. The device is useful for fast, scalable concentration enrichment. We anticipate the demonstration of simultaneous concentration enrichment and separation of different analytes in the near future.

The simulations show that, with a given buffer ionic strength, the tracer concentration in the enriched zone tends towards the same upper value regardless of reservoir concentration. The latter only determines the temporal domain of enrichment. At the same time, our results demonstrate that the enrichment factor alone does not allow the characterization and rigorous comparison of the efficiency of the investigated device in view of concentration enrichment. More comprehensively, the absolute concentration of enriched analytes and/or the preconcentration rate should be provided as more informative (and fair) parameters. Because the underlying mechanisms resulting in concentration enrichment are of a fundamental nature, this concern also addresses preconcentration steps in related devices.

Acknowledgements

This material is in part based upon work supported under a National Science Foundation Graduate Research Fellowship to RKP. We acknowledge the U.S. Department of Energy, Office of Basic Energy Sciences (Contract No. DE-FG02-06ER15758), and the Deutsche Forschungsgemeinschaft DFG (Bonn, Germany) for support of this work. Simulations were run at the "Leibniz-Rechenzentrum der Bayerischen Akademie der Wissenschaften" (Garching, Germany), supported by project HLRB pr26wo. We thank Prof. Henry S. White (University of Utah) for helpful discussions.

References

1 J. Lichtenberg, E. Verpoorte and N. F. de Rooij, *Electrophoresis*, 2001, **22**, 258–271.
2 R. L. Chien, *Electrophoresis*, 2003, **24**, 486–497.
3 Y. F. Shi, Y. Huang, J. P. Duan, H. Q. Chen and G. N. Chen, *J. Chromatogr., A*, 2006, **1125**, 124–128.
4 K. Sueyoshi, F. Kitagawa and K. Otsuka, *J. Sep. Sci.*, 2008, **31**, 2650–2666.
5 D. Ross and L. E. Locascio, *Anal. Chem.*, 2002, **74**, 2556–2564.
6 K. M. Balss, W. N. Vreeland, K. W. Phinney and D. Ross, *Anal. Chem.*, 2004, **76**, 7243–7249.
7 S. J. Hoebel, K. M. Balss, B. J. Jones, C. D. Malliaris, M. S. Munson, W. N. Vreeland and D. Ross, *Anal. Chem.*, 2006, **78**, 7186–7190.
8 S. M. Kim, G. J. Sommer, M. A. Burns and E. F. Hasselbrink, *Anal. Chem.*, 2006, **78**, 8028–8035.
9 H. Lin, J. G. Shackman and D. Ross, *Lab Chip*, 2008, **8**, 969–978.
10 P. Gebauer, W. Thormann and P. Bocek, *J. Chromatogr.*, 1992, **608**, 47–57.
11 M. Masar, M. Zuborova, D. Kaniansky and B. Stanislawski, *J. Sep. Sci.*, 2003, **26**, 647–652.
12 Z. Q. Xu, T. Nishine, A. Arai and T. Hirokawa, *Electrophoresis*, 2004, **25**, 3875–3881.
13 B. Jung, R. Bharadwaj and J. G. Santiago, *Anal. Chem.*, 2006, **78**, 2319–2327.
14 L. Chen, J. E. Prest, P. R. Fielden, N. J. Goddard, A. Manz and P. J. R. Day, *Lab Chip*, 2006, **6**, 474–487.
15 D. Kohlheyer, J. C. T. Eijkel, A. van den Berg and R. B. M. Schasfoort, *Electrophoresis*, 2008, **29**, 977–993.
16 A. E. Herr, J. I. Molho, K. A. Drouvalakis, J. C. Mikkelsen, P. J. Utz, J. G. Santiago and T. W. Kenny, *Anal. Chem.*, 2003, **75**, 1180–1187.
17 H. Cui, K. Horiuchi, P. Dutta and C. F. Ivory, *Anal. Chem.*, 2005, **77**, 1303–1309.
18 C. Li, Y. Yang, H. G. Craighead and K. H. Lee, *Electrophoresis*, 2005, **26**, 1800–1806.
19 B. Yao, H. Yang, Q. Liang, G. Luo, L. Wang, K. Ren, Y. Gao, Y. Wang and Y. Qiu, *Anal. Chem.*, 2006, **78**, 5845–5850.
20 V. Dauriac, S. Descroix, Y. Chen, G. Peltre and H. Senechal, *Electrophoresis*, 2008, **29**, 2945–2952.
21 R. D. Greenlee and C. F. Ivory, *Biotechnol. Prog.*, 1998, **14**, 300–309.
22 Q. G. Wang, S. L. Lin, K. F. Warnick, H. D. Tolley and M. L. Lee, *J. Chromatogr., A*, 2003, **985**, 455–462.
23 J. G. Shackman and D. Ross, *Electrophoresis*, 2007, **28**, 556–571.
24 K. F. Warnick, S. J. Francom, P. H. Humble, R. T. Kelly, A. T. Woolley, M. L. Lee and H. D. Tolley, *Electrophoresis*, 2005, **26**, 405–414.
25 D. N. Petsev, G. P. Lopez, C. F. Ivory and S. S. Sibbet, *Lab Chip*, 2005, **5**, 587–597.
26 R. T. Kelly and A. T. Woolley, *J. Sep. Sci.*, 2005, **28**, 1985–1993.
27 R. T. Kelly, Y. Li and A. T. Woolley, *Anal. Chem.*, 2006, **78**, 2565–2570.
28 J. K. Liu, X. F. Sun, P. B. Farnsworth and M. L. Lee, *Anal. Chem.*, 2006, **78**, 4654–4662.
29 C. Yu, M. H. Davey, F. Svec and J. M. J. Frechet, *Anal. Chem.*, 2001, **73**, 5088–5096.
30 A. B. Jemere, R. D. Oleschuk, F. Ouchen, F. Fajuyigbe and D. J. Harrison, *Electrophoresis*, 2002, **23**, 3537–3544.
31 B. S. Broyles, S. C. Jacobson and J. M. Ramsey, *Anal. Chem.*, 2003, **75**, 2761–2767.
32 D. L. Huber, R. P. Manginell, M. A. Samara, B. I. Kim and B. C. Bunker, *Science*, 2003, **301**, 352–354.
33 Y. Zhang and A. T. Timperman, *Analyst*, 2003, **128**, 537–542.
34 S. Song, A. K. Singh and B. J. Kirby, *Anal. Chem.*, 2004, **76**, 4589–4592.
35 S. Song, A. K. Singh, T. J. Shepodd and B. J. Kirby, *Anal. Chem.*, 2004, **76**, 2367–2373.
36 R. S. Foote, J. Khandurina, S. C. Jacobson and J. M. Ramsey, *Anal. Chem.*, 2005, **77**, 57–63.
37 Y.-C. Wang, A. L. Stevens and J. Han, *Anal. Chem.*, 2005, **77**, 4293–4299.
38 R. Dhopeshwarkar, L. Sun and R. M. Crooks, *Lab Chip*, 2005, **5**, 1148–1154.
39 S. Song and A. K. Singh, *Anal. Bioanal. Chem.*, 2006, **384**, 41–43.
40 S. M. Kim, M. A. Burns and E. F. Hasselbrink, *Anal. Chem.*, 2006, **78**, 4779–4785.
41 A. V. Hatch, A. E. Herr, D. J. Throckmorton, J. S. Brennan and A. K. Singh, *Anal. Chem.*, 2006, **78**, 4976–4984.
42 X. Jin, S. Joseph, E. N. Gatimu, P. W. Bohn and N. R. Aluru, *Langmuir*, 2007, **23**, 13209–13222.
43 A. Höltzel and U. Tallarek, *J. Sep. Sci.*, 2007, **30**, 1398–1419.
44 E. N. Gatimu, T. L. King, J. V. Sweedler and P. W. Bohn, *Biomicrofluidics*, 2007, **1**, 021502.
45 J. Han, J. Fu and R. B. Schoch, *Lab Chip*, 2008, **8**, 23–33.
46 D. Hlushkou, R. Dhopeshwarkar, R. M. Crooks and U. Tallarek, *Lab Chip*, 2008, **8**, 1153–1162.
47 K. M. Zhou, M. L. Kovarik and S. C. Jacobson, *J. Am. Chem. Soc.*, 2008, **130**, 8614–8616.
48 T. Kim and E. Meyhöfer, *Anal. Chem.*, 2008, **80**, 5383–5390.
49 C. F. Ivory, *Sep. Sci. Technol.*, 2000, **35**, 1777–1793.
50 C. F. Ivory, *Electrophoresis*, 2007, **28**, 15–25.
51 R. Dhopeshwarkar, D. Hlushkou, M. Nguyen, U. Tallarek and R. M. Crooks, *J. Am. Chem. Soc.*, 2008, **130**, 10480–10481.
52 A. Piruska, S. Branagan, D. M. Cropek, J. V. Sweedler and P. W. Bohn, *Lab Chip*, 2008, **8**, 1625–1631.
53 J. F. L. Duval, M. Minor, J. Cecilia and H. P. Van Leeuwen, *J. Phys. Chem. B*, 2003, **107**, 4143–4155.
54 J. F. L. Duval, G. K. Huijs, W. F. Threels, J. Lyklema and H. P. Van Leeuwen, *J. Colloid Interface Sci.*, 2003, **260**, 95–106.
55 S. Qian and J. F. L. Duval, *J. Colloid Interface Sci.*, 2006, **297**, 341–352.
56 T. M. Squires and M. Z. Bazant, *J. Fluid Mech.*, 2004, **509**, 217–252.
57 J. A. Levitan, S. Devasenathipathy, V. Studer, Y. Ben, T. Thorsen, T. M. Squires and M. Z. Bazant, *Colloids Surf., A*, 2005, **267**, 122–132.
58 K. T. Chu and M. Z. Bazant, *Phys. Rev. E: Stat., Nonlinear, Soft Matter*, 2006, **74**, 011501.
59 E. Yariv and T. Miloh, *J. Fluid Mech.*, 2008, **595**, 163–172.
60 W. Wei, G. Xue and E. S. Yeung, *Anal. Chem.*, 2002, **74**, 934–940.
61 J. C. McDonald, D. C. Duffy, J. R. Anderson, D. T. Chiu, W. Hongkai, O. J. A. Schueller and G. M. Whitesides, *Electrophoresis*, 2000, **21**, 27–40.
62 V. Videnova-Adrabinska, *Coord. Chem. Rev.*, 2007, **251**, 1987–2016.

63 J. Lyklema, *Fundamentals of Interface and Colloid Science, Vol. II: Solid-Liquid Interfaces*, Academic Press, London, 1995.
64 N. W. Ashcroft and N. D. Mermin, *Solid State Physics*, Saunders, Philadelphia, 1976.
65 A. Arora, J. C. T. Eijkel, W. E. Morf and A. Manz, *Anal. Chem.*, 2001, **73**, 3282–3288.
66 E. L. Littauer and K. C. Tsai, *Electrochim. Acta*, 1979, **24**, 351–355.
67 M. E. Abdelsalam, G. Denuault, M. A. Baldo, C. Bragato and S. Daniele, *Electroanalysis*, 2001, **13**, 289–294.
68 S. Daniele, M. A. Baldo, C. Bragato, M. E. Abdelsalam and G. Denuault, *Anal. Chem.*, 2002, **74**, 3290–3296.
69 I. Ciani and S. Daniele, *J. Electroanal. Chem.*, 2004, **564**, 133–140.
70 F. J. Higuera and J. Jiménez, *Europhys. Lett.*, 1989, **9**, 663–668.
71 P. B. Warren, *Int. J. Mod. Phys. C*, 1997, **8**, 889–898.
72 F. Capuani, I. Pagonabarraga and D. Frenkel, *J. Chem. Phys.*, 2004, **121**, 973–986.
73 B. J. Kirby and E. F. Hasselbrink, Jr., *Electrophoresis*, 2004, **25**, 203–213.